PHYSICAL REVIEW B **77**, 085116 (2008)

Two-step-wise interpretation of highly asymmetric, grazing angle (e,2e) on solids: A real momentum spectroscopy for surfaces and overlayers

A. Liscio,[1,2] A. Ruocco,[2] G. Stefani,[2] and S. Iacobucci[3,*]

[1]*CNR–Istituto Metodologie Inorganiche e Plasmi, Area della Ricerca di Roma, Via Salaria km 29.300, 00016 Monterotondo, Italy*

[2]*CNISM and Dipartimento di Fisica, Università di Roma Tre, Via Vasca Navale 84, 00146 Roma, Italy*

[3]*CNR–Istituto Sistemi Complessi, Area della Ricerca di Roma, Via Salaria km 29.300, 00016 Monterotondo, Italy*

(Received 19 January 2007; revised manuscript received 9 October 2007; published 20 February 2008)

This paper deals with the mechanism of grazing incidence (e,2e) events from surfaces. Two different approaches are considered. In both cases, elastic scattering with the crystal lattice assists the inelastic collision; these two steps are coupled either coherently or incoherently. Experimental evidence is given that the "coherent" approach reproduces better the cross section dependence on momentum transfer in the specific case of asymmetric kinematics at moderate electron energies. This model has allowed us to map out the band dispersion of the outermost valence states of highly oriented pyrolytic graphite and to measure the momentum distribution of π-electron states without invoking the contribution of reciprocal lattice vectors in the momentum conservation. Agreement between theory and experiment is satisfactory, though the presence of events where crystal momentum is reconstructed cannot be ruled out. These results, obtained with a significant reduction of the experiment duration by an implemented apparatus, show that reflection (e,2e) can be used to build up a momentum spectroscopy with high surface sensitivity.

DOI: 10.1103/PhysRevB.77.085116 PACS number(s): 71.20.−b, 13.85.Fb

I. INTRODUCTION

The spectral momentum density of an electron state is the square modulus of the wave function in the momentum space $\rho(\vec{q},\epsilon)=|\Psi(\vec{q},\epsilon)|^2$, where $\vec{q}$ and ϵ are the momentum and the binding energy, respectively. It provides information about the different states of aggregation of matter that is more detailed than the one usually obtained by binding energy aimed spectroscopies.[1–3] This is because momentum density is more sensitive than binding energy to the long range part of the Coulomb interaction, hence to the diffused part of the electron wave function. In this respect, while providing a test bed for theoretical models, $\rho(\vec{q},\epsilon)$ can be suitably used to shed light on the properties of complex aggregates. In particular, the momentum density is an observable potentially relevant to characterize chemical reactivity[4] and, as a consequence, to control the interaction mechanism driving the synthesis of new materials.

Several spectroscopies permit us to measure $\rho(\vec{q},\epsilon)$ with various degrees of approximation. The binding energy–integrated momentum density $\int_0^{\vec{q}max}\rho(\vec{q})d\vec{q}$ (i.e., summed over all occupied bound states and integrated over a given momentum interval) is obtained by Compton scattering,[5] while in positron annihilation $(e^+e^-,\gamma'\gamma)$ the information on the fully differential $\rho(\vec{q},\epsilon)$ is obtained but limited to the Fermi level.[6] The ability to gain differential information on both energy and momentum can be obtained only by applying coincidence techniques that measure both final particles produced in a photon-impact $(\gamma,\gamma' e)$ or an electron-impact ionization event (e,2e).[7] Among them, the (e,2e) spectroscopy (one electron in–two electrons out) is the one that has been more extensively applied to study bulk and surface properties of solids.[1]

In an (e,2e) event, an incident electron impinges on a target electron with a subsequent emission of two electrons, which are detected in coincidence and at well defined angles and energies. The (e,2e) technique is well established, making use of transmission kinematics and high-energy primary electrons ($E>10$ keV).[8] By labeling the primary, fast scattered, and slow emitted electrons by the indices 0, s, and e, respectively, the energy and the momentum conservation of the (e,2e) process can be written as

$$E_0+\varepsilon(\vec{q})=E_s+E_e+\mathrm{WF},$$

$$\vec{k}_0+\vec{q}=\vec{k}_s+\vec{k}_e+\vec{g}, \tag{1}$$

where $\vec{k}_{0,s,e}$ and $E_{0,s,e}$ are wave vectors and energies of the three free electrons in the vacuum and WF is the work function of the solid. In Eq. (1), the momentum conservation is strictly valid for the component parallel to the surface. The refraction of electrons at the surface barrier can be taken into account by correcting the perpendicular component of each wave vector $k_i^{\perp}=(2m/\hbar^2)[E_i \sin^2\theta_i+U_0]^{1/2}$, $(i=0,s,e)$, where E_i is the kinetic energy measured in vacuum, θ_i is the angle with respect to the surface of the sample, and U_0 is a suitable value for the inner potential derived from independent measurements.[9] Within the frame of the plane wave impulse approximation (PWIA),[1] the momentum opposite to the recoil ion momentum is, in accordance with Eq. (1), interpreted as the bound electron momentum, and in the case of a crystalline target it is related to the bound electron crystal momentum up to a reciprocal lattice vector $\vec{g}$. Hence, the binding energy and the momentum of the bound electron state can be determined by kinematical arguments.

Performing experiments at high-momentum transfer ($\vec{k}=\vec{k}_0-\vec{k}_s\approx\vec{k}_e$), the impulse approximation (IA) is valid, and the momentum space wave function can be probed.[10] This corresponds to a generic band b_j whose spectral momentum density is peaked in the jth zone to measure only the contribution corresponding to the (real) momentum selected according to the momentum conservation without relying on $\vec{g}$.

Contributions to the measured intensity that may come from all Brillouin zones[11] are due to $\vec{g}$-assisted events, their relevance being related to the (de-)localization of the ionizing collision, that is, to the IA validity. Furthermore, it is an easy matter to see from Eq. (1) that the possibility of varying arbitrarily the momentum transfer allows spanning $\vec{q}$ even for $\vec{g}=\vec{0}$. Hence, differently from photoemission, (e,2e) allows us to map out the energy vs momentum dispersion relationship at low momenta without relying on the crystal momentum. This opens up the possibility of measuring the electronic structure in nonperiodic solids, such as polycrystals, clusters, molecules deposited on surfaces assembling not in register with the substrate periodicity, etc.[12]

It has been demonstrated that to study surfaces and overlayers (such as clean surfaces of real samples, adsorbates, etc.), the reflection geometry and the use of electrons with kinetic energies of a few hundreds of eV are appropriate[13] due to the short probing depth of these kinematics.[14] Furthermore, the detection in coincidence of the electron pair in the final state results in a probing depth that is smaller than the corresponding "single" experiments, where only one of the two free electrons is revealed. This has been recently shown in Auger-photoelectron coincidence experiments, which are characterized by two-electron final states similar to the one of the reflection (e,2e) performed at intermediate energy.[15,16] However, in this energy regime, the electron-solid interactions, such as periodical distortion of the electron motion in the vacuum due to the interaction with the bulk potential[17] and excitation of collective electron modes (both extrinsic and intrinsic losses), become relevant.[18] In general, these effects prevent disentangling of dynamic effects from electronic properties of the target in the (e,2e) cross section. Nevertheless, under proper conditions, an insight into the target electronic structure can be provided by the cross section measured by these experiments. As shown in Ref. 19 by reflection (e,2e) performed at a few hundreds of eV and grazing incidence kinematics, the dispersion curves of the highly oriented pyrolitic graphite (HOPG) valence states were measured and a fair agreement between the experimental and the calculated momentum density of the π band was found. At lower energies and by spin polarizing the electron source, the two-electron coincidence technique allowed for an insight into the spin-split electronic band structure of Fe (100) surface, and it was shown to be suitable to investigate the electrons' exchange scattering at surfaces.[20]

In reflection kinematics, the probability for a single-scattering event is associated with very large $\vec{k}$; hence, a two-step process, in which a further interaction with the solid is involved for emitting the electron pair into the vacuum, may dominate over the single-scattering one.[21] This was demonstrated by Iacobucci *et al.* for reflection (e,2e) performed at moderate incident energies[22] and by Artamonov *et al.* for (e,2e) performed at low kinetic energies in backscattering geometry.[23] In both cases, the cross section showed symmetry with respect to the direction of the specularly reflected rather than the direct incident beam. On this base, the ejection of the correlated electron pair requires that an elastic event producing the mirror reflection assists the inelastic event that knocks out the bound electron. Once the ionizing collision has taken place, then the electron pair propagates to the surface and escapes into the vacuum, with a mechanism conceptually similar to the one adopted for the volume photoionization from solids.[9]

The main purpose of this paper is to gain a better insight into the mechanism of the reflection (e,2e) process in order to explore its capability to measure the momentum density of solids in general and of surfaces in particular. We have carried out an extensive investigation on the grazing angle (e,2e) cross section upon asymmetric kinematics—i.e., with unequal sharing of the energy between the final electrons—at moderate kinetic energies, where surface sensitivity is enhanced. In this kinematics, the minimum momentum, transferred through the inelastic collision in the two-step process, is five times smaller than the one needed to fully satisfy the IA but is 2 orders of magnitude larger than the momentum of an equivalent adsorbed photon (with energy equal to the energy transfer ΔE), i.e., dipole approximation conditions. We then assume IA to be better suited to describe our experiments and have accordingly written the differential cross section. Hence, an interpretation of our experiment will be made following the footprints of previous works on transmission (e,2e).[8,12]

We have calculated the cross section for the specific kinematics of this work starting from the general theory of electron pair emission from solids proposed in Refs. 18 and 24. We show that, in spite of the two-step model, the measured cross section can be factorized in a structure term and a dynamic one, and upon appropriate approximations, it is possible to extract the spectral momentum density. This peculiar spectroscopic information makes reflection (e,2e) a complementary technique to angle-resolved photoemission spectroscopy (ARPES) in studying surface electronic properties. ARPES can determine with great detail the electronic structure of surface systems;[25] in particular, the energy vs crystal-momentum dispersion relationship is measured with excellent energy and momentum resolutions, though applications are often limited to systems with long range periodicity.[26] Nonetheless, detailed information on the electron momentum distribution cannot be directly obtained by ARPES due to the delocalization of the photoemission event, this being well described by the dipole approximation.

With the goal of determining the validity of the model used to derive the (e,2e) cross section, as a testing case we have used electrons with kinetic energies of about 300 eV incident on a well known system as the (0001) surface of HOPG. The kinetic energy was nearly the same for the fast scattered electron and a few tens of eV for the slow one (see Fig. 1 for a sketch of the kinematics used in the experiment). From the dependence of the cross section on $\vec{k}$, two models have been compared with angle-dependent experiments, the differences being in the degree of accuracy by which the electron interaction with the sample is accounted for. Then, we have used the developed model to interpret the results of a series of energy-dependent experiments performed at a fixed geometry: We have measured the valence-band dispersion and extracted the electron momentum density for the HOPG outermost bound states.

The rest of the paper is organized as follows. In the second paragraph, the cross section for the reflection (e,2e) is

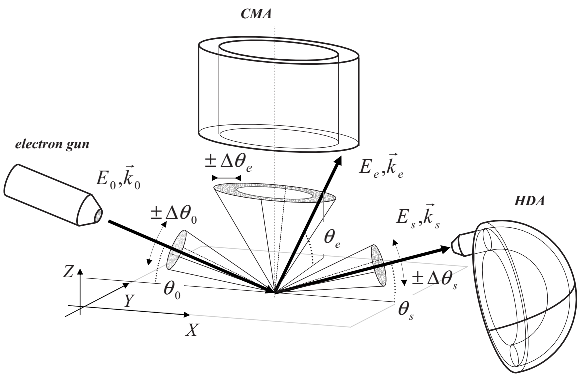

FIG. 1. Schematic representation of the grazing angle reflection (e,2e) experiment. The electron gun produces the primary electron (labeled by "0") that impinges onto the target surface. The two outgoing electrons (the scattered s and the emitted e) are detected by the HDA and CMA, respectively. Their energies and momenta are indicated by E_i and $\vec{k}_i$ $(i=0,s,e)$. The arrows represent the directions of the three electron beams in the hypothesis of infinitesimal angular acceptance of the spectrometer; the shaded areas show the finite angular acceptance ranges ($\Delta\theta' s$). The laboratory reference system is also displayed.

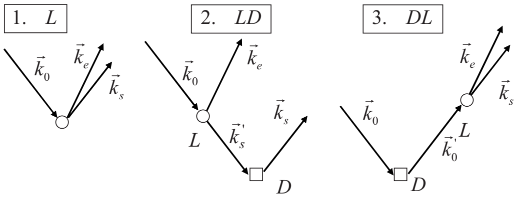

FIG. 2. The three sequences describing the first order of the (e,2e) transition operator. Sequence 1 describes the electron-electron scattering process as a single event L at large momentum transfer. Sequences 2 and 3 describe a double mechanism, where the inelastic electron-electron scattering (L) is assisted by an elastic scattering (D). In the sequence LD (DL), the fast electron undergoes elastic scattering with large momentum transfer after (before) the inelastic one with the bounded electron occurring at small momentum transfer.

derived for asymmetric kinematics at moderate electron energies. In the third section, the experimental aspects are presented, with particular attention to the implications due to the long acquisition times for measuring the multiply differential (e,2e) cross section. The limitations related to both instrumentation and sample stability (surface lifetime) have been overcome by implementing the reflection (e,2e) apparatus used by Iacobucci *et al.*[27] with multichannel parallel detection (in energy for the fast electron, in angle for the slow one). The experimental data are reported, analyzed, and discussed in the fourth section. Finally, the results and the conclusions are summarized.

II. THEORETICAL APPROACH

The differential cross section for (e,2e) processes in solids (DCSS) can be written, within a two-body interaction approximation, as[24]

$$\frac{d^6\sigma}{dE_s d\Omega_s dE_e d\Omega_e} \propto \frac{k_s k_e}{k_0} \sum_{j_{occ}} |\langle \vec{k}_s, \vec{k}_e | T_{(e,2e)} | \vec{k}_0, \vec{q}_j \rangle \times \langle \psi^I | \psi^{N-1} \rangle|^2 \delta_{\varepsilon_j, E_e+E_s-E_0}, \qquad (2)$$

where the sum is over all the spin states, which are not resolved in the experiment. The directions of the two ejected electrons are specified by the two solid angles Ω_s and Ω_e. The two state vectors $|\vec{k}_0, \vec{q}_j\rangle$ and $|\vec{k}_s, \vec{k}_e\rangle$ describe the initial and the final asymptotic electron states, respectively. The bracket $|\langle \psi^I | \psi^{N-1} \rangle|^2$ is the probability that the removal of an electron from the jth state $|\vec{q}_j\rangle$ of the N-electron ground state leaves the system in the ionized $|\psi^I\rangle$ state of the residual $N-1$ electron system; $|\langle \psi^I | \psi^{N-1} \rangle|^2 = \delta_{I,N-1}$ in the frozen-core approximation.[28] The sum is performed over all the occupied one-particle valence states of the target $|\vec{q}_j\rangle$, with energy ε_i given by the Dirac-δ function. All the interactions leading to the (e,2e) process are included in the operator $T_{(e,2e)}$.[24] Asymmetric kinematics ($E_0 - E_s \ll E_0$) allow us (i) to neglect the exchange in the final state and (ii) to consider solid-electron and electron-electron interaction only to the first order.[17] In the frozen-core approximation, the (e,2e) operator takes the form

$$T_{(e,2e)} = (1 + V_e G_e)(W_{se} + V_s g_s' W_{se} + W_{se} g_0' V_s), \qquad (3)$$

where V_s and V_e are effective potentials accounting for all possible scattering events with the solid that assist the electron-electron scattering described by W_{se}. In Eq. (3), G_e is the propagator of the emitted electron in the potential V_e; g_0' and g_s' are the free electron propagators at kinetic energies E_0 and E_s, respectively. Surface discontinuity is accounted for by a complex inner potential describing electron refraction and absorption inside the solid,[17] and recall that within the PWIA the recoil momentum $\vec{q}$ can be interpreted as the bound electron momentum $\vec{q}_j$.[1] Using Eq. (3), the general form of the (e,2e) cross section in Eq. (2) becomes

$$\frac{d^6\sigma}{dE_s d\Omega_s dE_e d\Omega_e} \propto \frac{k_s k_e}{k_0} \sum_{j_{occ}} |\langle \vec{K}_e | F(\vec{k}_0, \vec{k}_s) | \vec{q}_j \rangle|^2 \delta_{\varepsilon_j, E_e+E_s-E_0}, \qquad (4a)$$

$$F(\vec{k}_0, \vec{k}_s) = \langle \vec{k}_s | W_{se} + V_s g_s' W_{se} + W_{se} g_0' V_s | \vec{k}_0 \rangle = F_D + F_{LD} + F_{DL}. \qquad (4b)$$

The matrix element F can be regarded as an effective one-electron transition operator that projects the initial valence state $|\vec{q}_j\rangle$ onto the final state $\langle \vec{K}_e | = \langle \vec{k}_e | (1 + G_e^- V_e)$, that is, the time-reversed scattering state of the emitted electron. $F(\vec{k}_0, \vec{k}_s)$ consists of three terms, which we have labeled L, LD, and DL, respectively. The L term describes the electron-electron scattering process as a single event occurring at large momentum transfer. The LD (DL) term describes a double collision, where the electron-electron scattering is assisted by a single elastic scattering from the crystal potential V_s, occurring after (before) the inelastic interaction W_{se} with the bound electron. The three scattering sequences associated with the three terms are schematically shown in Fig. 2. Expression (4a) can be written as

$$\frac{d^6\sigma}{dE_s d\Omega_s dE_e d\Omega_e} \propto \frac{k_s k_e}{k_0} \sum_{j_{occ}} \left| \left\langle \vec{K}_e \left| \sum_{t=1}^{3} F_t \right| \vec{q}_j \right\rangle \right|^2 \delta_{\varepsilon_j, E_e+E_s-E_0}, \tag{5}$$

where the index $t=1,2,3$ labels the three different sequences L, LD, DL, respectively.

The computation of the (e,2e) transition amplitude that appears in Eq. (5) is simplified when the incoherent sum of the three scattering amplitudes can be performed. The validity of this assumption is supported by results of elastic and inelastic I-V experiments[29] performed in reflection geometry on the HOPG surface at a few hundreds of eV incident energy, where a kinematical model with independent sequential collisions was sufficient to account for the features observed in the measured cross section. On the other hand, reliability on incoherent summation can be explained considering that the DL and the LD sequential paths end up to the same final state for the two free electrons but, on the basis of the dependence of the cross section on q_z, they reconstruct two different q values for the initial bound state. Hence, even in the frozen-core approximation, the initial state of the two sequences is different, and no interference between the two amplitudes is expected. Under this assumption, the square modulus of the scattering amplitude is simplified in

$$\left| \left\langle \vec{K}_e \left| \sum_{t=1}^{3} F_t \right| \vec{q}_j \right\rangle \right|^2 = \sum_{t=1}^{3} |\langle \vec{K}_e | F_t | \vec{q}_j \rangle|^2. \tag{6}$$

We describe a valence state in plane wave terms, whose Bloch function is

$$\Psi_{j,Bloch} = \langle \vec{r}_e | \vec{q}_j \rangle \propto \sum_{\vec{g}} c_{\vec{q}_j - \vec{g}} \exp\{i(\vec{q}_j - \vec{g}) \cdot \vec{r}_e\}, \tag{7}$$

where $c_{\vec{g}_j-\vec{g}}$ is the Bloch coefficient, and its square modulus is proportional to the density of occupied states ρ_i of the target. ARPES provides experimental evidence that the emitted slow electron can be described as a plane wave modulated by the density ρ_{unocc} of unoccupied states.[30,31] Hence, in the spirit of the PWIA, we approximate the emitted electron wave function by the form

$$\Psi_e = \langle \vec{r}_e | \vec{K}_e \rangle \propto c(\vec{k}_e) \exp\{i\vec{k}_e \cdot \vec{r}_e\}, \quad |c(\vec{k}_e)|^2 \propto \rho_{unocc}(\vec{k}_e), \tag{8}$$

where we have reduced the effective electron-solid potential V_e to the Coulomb electron-ion interaction summed over all the lattice sites. By assuming the crystal potential V_s as a superposition of screened-Coulomb potentials of the ionic cores,[18] the (e,2e) cross section takes the form

$$\frac{d^6\sigma}{dE_s d\Omega_s dE_e d\Omega_e} \propto \frac{k_s k_e}{k_0} \sum_{t=1}^{3} \Gamma_t(\vec{k}_0, \vec{k}_s, \vec{k}_e) \cdot \rho^t_{unocc}(\vec{k}_e) \cdot \left[\sum_{j_{occ}} \rho^t_j \delta_{\varepsilon_j, E_e+E_s-E_0} \right]. \tag{9}$$

The cross section is the incoherent sum of three terms; the two collisions (elastic and inelastic) contributing to the second and the third term are treated in a coherent mode. Each term of the sum appearing in Eq. (9) is factorized in two parts: a kinematical factor Γ_t and a structure term, similar to the cross section valid for high-energy (e,2e) transmission experiments.[32] Nonetheless, while at high energy, the structural factor coincides with the momentum density of the initial bound state; in this case, it is modulated by the momentum density $\rho^t_{unocc}(\vec{k}_e) = |c(\vec{k}_e)\, \delta_{\vec{k}_e, \vec{k}_0+\vec{q}_j-\vec{k}_g+\vec{g}}|^2$ of the unoccupied states with momentum $\vec{k}_e$. This density of states is not measured by the (e,2e) experiment and should be estimated from calculations or derived by independent measurements, such as secondary electron emission (SEE) spectroscopy.[33] Furthermore, in Eq. (9) the kinematical factors Γ_t, whose analytical expression is given in Ref. 18 (see Appendix A for full details), summarize all information on the one-electron interactions. In the present case, to evaluate Γ_t we have neglected the image-charge interaction and, instead of a Jellium model, we have used a quasi-free-electron approximation to describe both the bound and the emitted electron. It is worth noticing that a factorization analogous to the one of Eq. (9) is obtained also for a tight binding model.[34]

In previous works, performed with the same kinematics as in the present experiment,[13,19,27] both quasi-free-electron approximation and independence of the three collision sequences were used as well. Only the DL sequence was accounted for to describe the (e,2e) process, and elastic and inelastic collisions acted as two independent events. Namely, the elastic interaction with the solid simply resulted in varying the direction of the incident beam (reflection).[21] Introducing incoherency between the elastic and inelastic steps in the present formulation of the (e,2e) cross section results in changing the matrix element F_{DL} in Eq. (4a) with the product of the matrix elements of the two scattering events: the elastic (F_D) and the inelastic (F_L). The matrix element F_L can be regarded as an effective one-electron transition operator that projects the initial valence state onto the final (distorted) state of the emitted electron. The square modulus of F_D is the probability of the elastic reflection. Hence, the cross section of the DL sequence reduces to the elastic scattering cross section[17] multiplied by the (e,2e) expression calculated by Kheifets *et al.*,[21]

$$\left. \frac{d^6\sigma}{dE_s d\Omega_s dE_e d\Omega_e} \right|^{indep}_{DL} \propto \frac{k_s k_e}{k_0} \cdot |S_{\vec{k}'_0-\vec{k}_0}|^2 \cdot \Gamma_D(\vec{k}'_0, \vec{k}_0) \Gamma_L(\vec{k}'_0, \vec{k}_s) \cdot \rho_{unocc}(\vec{k}_e) \cdot \left[\sum_{j_{occ}} \rho_j \delta_{\varepsilon_j, E_e+E_s-E_0} \right], \tag{10}$$

where $\vec{k}'_0$ is the momentum of the fast electron between elastic and inelastic scattering; the kinematical factors $\Gamma_D(\vec{k}'_0, \vec{k}_0)$ and $\Gamma_L(\vec{k}'_0, \vec{k}_s)$ are the square modulus of the Fourier transforms of the interaction potentials. In the case of screened-Coulomb potential, the kinematical factors take the $[k^2+\lambda^2]^{-2}$ form, where k is the module of the momentum transferred in each scattering events and λ is the inverse of the screening length.[35] The term $|S_{\vec{k}'_0-\vec{k}_0}|^2$ accounts for the periodicity breakdown of the crystal potential at the surface. It is worth noticing that the structure term in Eq. (10) is the same as in Eq. (9). For the conjugated *LD* process, a formula analogous to Eq. (10) holds and, as in the case of the (e,2e) cross section derived in Eq. (9), two different structural factors are associated with the two corresponding sequential paths. Actually, the two sequences *LD* and *DL* are equivalent, provided that the experiment is performed in a strictly mirror geometry (i.e., $\theta_0 = \theta_s$): Only in this specific setup does the *LD* sequence reconstruct the same momentum as the *DL* one. In summary, the main difference between Eqs. (9) and (10) is the degree of accuracy used in accounting for the interaction of the electrons with the solid, this being reflected in the different form of the kinematics factor calculated in the two cases.

III. EXPERIMENT

The apparatus operates at a small grazing angle, thus allowing us to enhance the surface sensitivity of electrons with intermediate kinetic energies. It is an evolution of the one used by Rioual *et al.* to perform the first momentum distribution measurement of a solid sample in reflection geometry.[19] Iacobucci *et al.*[27] have already shown that the use of angle-multichannel detection for the slow emitted electrons improves the momentum resolution of the coincidence apparatus without degrading the overall luminosity. The Achille's tendon of coincidence measurements is the long acquisition time, which cannot be reduced by increasing the flux of the primary electrons.[36] In order to reduce it from a few days to tens of hours, a value which is compatible with the reactivity of the sample in ultrahigh-vacuum (UHV) conditions, we have implemented the energy-multichannel detection for the fast scattered electrons.

A schematic representation of the fully multichannel apparatus is shown in Fig. 1. A detailed description can be found elsewhere.[37] Briefly, the electron gun produces a few hundreds of eV beam, which impinged at a grazing angle on the sample; the fast scattered and the slow emitted electrons are detected in coincidence by two electrostatic analyzers, a hemispherical deflection analyzer (HDA) and a cylindrical mirror analyzer (CMA). To achieve parallel acquisition, both of them have been equipped with two-dimensional position sensitive detectors (PSDs). The full description of the coincidence electronics for experiment control and acquisition is described in Ref. 37. Typical energy and the momentum resolution achieved are 1.3 eV and 0.15 Å^{-1}, respectively. These quantities are mean values; more details are given in the following paragraph.

As a target, we have used the (0001) surface of a commercial HOPG sample of ZYA quality (Surface Preparation Laboratory, Zaandam, The Netherlands), whose alignment along the $\hat{c}$ axis was better then 0.2°, prepared in UHV according to the method described in Ref. 38. We have checked its surface cleanliness and order by measuring the angle distribution of elastically scattered electrons, as well as by measuring reflection electron energy loss spectroscopy and SEE distributions. These measurements have given evidence for surface stability (clearness and wrinkleless) over a 1 week period, which is larger than the one needed for (e,2e) experiments.

A. Phases space sampled by the spectrometer

The PSD's outputs have been binned into sets of channels whose dimensions are determined by the energy resolution ΔE and by the momentum resolution Δq that one wants to achieve. The main contribution to ΔE comes from the energy resolution of the HDA, i.e., 0.9 eV, as measured in noncoincident multichannel mode, which results to 1.3 eV in coincidence experiments by regrouping the energy channels into ten independent bins. The main contribution to Δq corresponds to the CMA angle resolution $\Delta\Omega$, which is obtained by dividing its azimuth acceptance into 12 slices of 30° each.[37] These values are a compromise between the resolutions that one wants to achieve and the reasonable values of the coincident count rate. The bins, time correlated into couples, generate 120 coincidence channels. Each channel given by the binning procedure corresponds to a constant volume $\Delta\Omega \times \Delta\varepsilon$. However, the transformation of the angle-energy space into the momentum–binding energy phase space does not conserve the volume. Each bin couple samples a different volume $\Delta q \times \Delta\varepsilon$ of the phase space with associated centroid values $\langle q \rangle$ and $\langle \varepsilon \rangle$.

A procedure has been developed to calculate the values of volumes and centroids. We have simulated our experiment, having finite angle-energy resolutions, as a collection of experiments with infinitesimal resolutions. In our experimental conditions, the energy resolution effect is six times smaller than the angular acceptance effect; hence, we have taken into account only the angular effects and simulated the acceptance effects over the momentum space. To this end, we have described each electron channel [i.e., primary (0), scattered (s), and ejected (e)] as a wave-vector array $\underline{\vec{k}_l} = \{\vec{k}_{l,1}, \vec{k}_{l,2}, \ldots, \vec{k}_{l,N_t}\}$ $(l=0,s,e)$, where N_t is the number of the array components, and each component represents the electron wave vector in the case of infinitesimal angular acceptance. The array shapes of both the primary and the scattered electrons are spherical sectors, and the array shape of the ejected electron (over all the azimuthal directions) is a conical crown, as shown in Fig. 1. Each HDA bin has been simulated by using the wave-vector array shape of the scattered electrons having the corresponding bin energy. Let us consider the plane perpendicular to the symmetry axis of the l array. We have divided this plane by a constant step grid, where the nodes identify the projection of the $\underline{\vec{k}_l}$ wave-vector vertexes. In this way, the discrete angle distribution of the three electron channels have been calculated for each of the respective N_0, N_s, and N_e elements according to momentum and energy conservation. We have extracted the measured recoil momentum $\langle \vec{q} \rangle$ by averaging over the recoil momenta $\vec{q}_h$, each $\vec{q}_h$ being given by the momentum conservation law of individual (e,2e) kinematics (momenta tern) obtained by combining the wave vectors of the three arrays $(0, s, e)$,

$$\langle \vec{q} \rangle = \frac{\sum_{i=1}^{N_0}\sum_{m=1}^{N_s}\sum_{n=1}^{N_e}[\vec{k}_{s,m}+\vec{k}_{e,n}-\vec{k}_{0,i}]}{N_0\times N_s\times N_e} = \frac{\sum_{h=1}^{N_{tot}}\vec{q}_h}{N_{tot}} = \sum_{h=1}^{N^{ne}} f_{\Delta\Omega,h}\cdot\vec{q}_h, \tag{11a}$$

where

$$\sum_{h=1}^{N^{ne}} f_{\Delta\Omega,h}=1 \quad \Delta q|_{x,y,z} = \sqrt{\frac{1}{N_{tot}}\sum_{h=1}^{N_{tot}}[\langle q\rangle - q_h]^2}\,\Bigg|_{x,y,z}, \tag{11b}$$

where i, m, and n index the elements of each array. $N_{tot}=N_0\times N_s\times N_e$ is the total number of the terns given by all the combinations of the components of the three wave-vector arrays; namely, it is the total number of individual kinematics corresponding to experiments with infinitesimal acceptance. As different momenta terms may give rise to the same $\vec{q}$, in Eqs. (11a) and (11b) we have introduced the "discrete probability density" $f_{\Delta\Omega,h}$. It represents the relative weight of the momentum $\vec{q}_h$ sampled by each nonequivalent tern (the total number of these terns being N^{ne}), and it is determined by the experimental acceptance. The variance of the $f_{\Delta\Omega,h}$ distribution, given by $\Delta q|_{x,y,z}$, varies less than 10% for a step of the wave-vector array of 0.05 Å^{-1}.

By averaging over the N_{tot} differential (e,2e) cross sections Y_h with infinitesimal angular acceptance, we extract the measured cross section $\tilde{Y}_{(e,2e)}$,

$$\tilde{Y}_{(e,2e)} \propto \frac{1}{N_{tot}}\sum_{h=1}^{N_h}\frac{d^6\sigma}{dE_s d\Omega_s dE_e d\Omega_e}\Bigg|_h = \frac{1}{N^{ne}}\sum_h f_{\Delta\Omega,h}Y_h, \tag{12}$$

which is obtained by using the weight function $f_{\Delta\Omega,h}$.

The quantitative relevance of these considerations is found in the analysis of valence-band mapping measurements (see next section). We have performed a series of (e,2e) experiments, which sample binding energies and parallel and perpendicular momenta in the ranges $0<\varepsilon<15.4$ eV, $0.3<q_\parallel<2$ Å^{-1} and $2.2<q_z<2.8$ Å^{-1}, respectively (as usually defined in surface studies, $\vec{q}$ is decoupled in perpendicular and parallel components with respect to the surface plane). While the experiment measures momenta outside the solid, to evaluate the (e,2e) cross section we have described the electron scattering events inside the solid; hence, to calculate the perpendicular momentum, we have accounted for the surface discontinuity by using a complex inner potential $U_0=(15.6+7i)$ eV, describing electron refraction and absorption.[29] We have used specular reflection geometry ($\theta_0=\theta_s=6.0\pm0.5°$), primary electrons with kinetic energies $318\leqslant E_0\leqslant 334$ eV, and ejected electrons with energy $6\leqslant E_e\leqslant 22$ eV. During each (e,2e) measurement, the kinetic energies of both the primary and the ejected electron were fixed, while scattered electrons of 300 ± 5 eV were simultaneously measured within the accepted range of the multichannel detector.[37]

As an example, Fig. 3 plots the projection onto the $(q_\parallel,\varepsilon)$ plane of the phase space sampled in a measurement taken for $E_0=318$ eV and $E_e=6$ eV. Each data point is given by the centroid of energy $\langle\varepsilon\rangle$ and momentum $\langle q_\parallel\rangle$, reconstructed according to Eqs. (11a) and (11b), within each individual bin. In Fig. 3, the squares of unbiased estimate variance for the reconstructed parallel momentum $\Delta q_\parallel$ are reported as error bars; we notice that the variance depends on both energy and momentum, and it varies in the range $0.05<\Delta q_\parallel<0.10$ Å^{-1}.

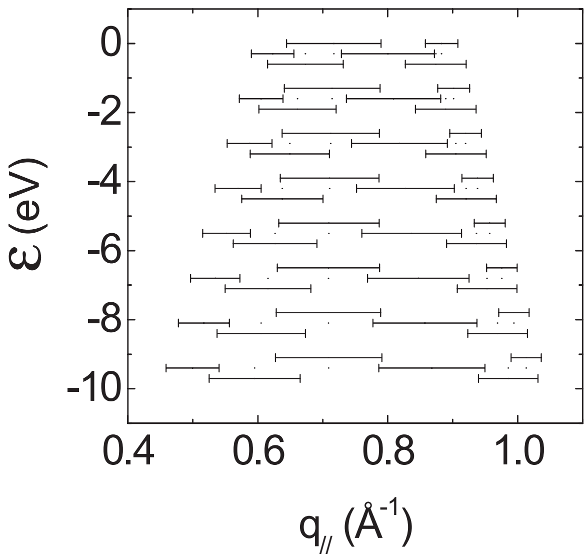

FIG. 3. Phase-space $(q_\parallel,\varepsilon)$ sampled by a multichannel (e,2e) experiment performed in specular reflection geometry ($\theta_0=\theta_s=6.0°$) for fixed kinetic energies of the primary electron ($E_0=318$ eV) and of the ejected electron ($E_e=6$ eV). During the measurement, the scattered electrons of 300 ± 5 eV were simultaneously measured within the accepted range of the multichannel detector. The positions of the experimental data are given by the centroids of energy $\langle\varepsilon\rangle$ and parallel momentum $\langle q_\parallel\rangle$ of each bin calculated according to Eqs. (11a) and (11b). The bars represent the estimate variances of the discrete probability densities ($f_{\Delta\Omega,h}$).

An example of the $f_{\Delta\Omega,h}$ distribution is given in Fig. 4. The primary electron impinged onto the sample surface with kinetic energy $E_0=(321.05\pm0.05)$ eV and grazing angle $\theta_0=7.5°$. The ejected electron, with kinetic energy $E_e=(10.0\pm0.2)$ eV, was collected at a fixed polar angle $\theta_e=42.3°$ and over the entire azimuth angle. The scattered electron, with kinetic energy $E_s=(300.5\pm0.5)$ eV, was collected by scanning θ_s over the angular range $1°<\theta_s<12°$. The histograms reported under the bottom axis correspond to the measured $f_{\Delta\Omega,h}$ distribution. It is worth noticing that this function is neither uniform nor symmetric, but it has two distinct structures at the edge, and then the corresponding measured momenta may not coincide with the distribution mean values. This fact underlines the importance to simulate the effects of the spectrometer angular acceptance.

To summarize, the performances of the experimental apparatus are enhanced in the parallel multichannel-acquisition mode: Calculated according to Eqs. (11a) and (11b), an average parallel momentum resolution of 0.07 Å^{-1} has been achieved. The multichannel acquisition of scattered electrons has allowed us to increase the detected energy range by a factor of 10 without degrading the energy resolution (1.3 eV), hence to reduce the acquisition time by an order of

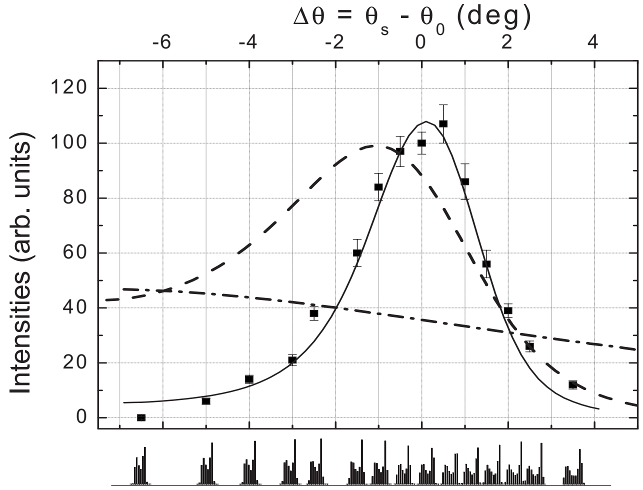

FIG. 4. Main figure: angle distribution of the scattered electrons (squares) measured with kinetic energy of 301 eV, fixed polar angle ($\theta_e = 48 \pm 3°$), and integrated over the azimuthal angle. The primary electron energy is 321 eV. The distribution is a function of the angular variation with respect to the specular angle ($\Delta\theta = \theta_s - \theta_0$) and is compared to the theoretical cross section (line) accounting of the experimental acceptances. Each theoretical distribution is calculated for three different descriptions of the (e,2e) scattering event: *L* sequence, single inelastic scattering (dot-dashed line); *LD* and *DL* sequences, elastic scattering assisted by an inelastic one described as two coherent events (solid line) and incoherent events (dashed line). Each theoretical distribution is fitted to the experimental data using a scale factor as the only free parameter. Bottom figure: discrete probability densities ($f_{\Delta\Omega,h}$) given by the experimental acceptances. They represent the relative weight of the momenta sampled by each experimental data (see text for details).

magnitude with respect to the single-channel-acquisition mode.

IV. EXPERIMENTAL RESULTS AND DISCUSSION

In the following paragraphs, we present and discuss two sets of reflection (e,2e) experiments. The first set of angle-integrated measurements are relevant in determining the reliability of the theoretical model discussed in Sec. II. In the second set of angle-resolved (e,2e) measurements, we exploit the model to interpret the results of valence-band mapping experiments.

A. Dependence of the differential cross section on momentum transfer

We have studied the dependence of the differential cross section (DCSS) on momentum transfer by measuring the coincidence angular distribution of electron pairs as a function of the scattering angle θ_s (see the geometrical setup in Fig. 1).

In Fig. 4, the measured DCSS (squares) is reported as a function of the variation of the scattering angle $\Delta\theta$ with respect to the specular reflection angle θ_0 (i.e., $\Delta\theta = \theta_s - \theta_0$). From the energy conservation law [Eq. (1)] in which WF=4.5 eV is assumed, the selected binding energy is $\varepsilon = (6.0 \pm 0.5)$ eV. The angular distribution shows a weak asymmetry with respect to a maximum, which corresponds to the specular reflection ($\Delta\theta \approx 0°$).

Using Eqs. (11a) and (11b), we have calculated the parallel momentum $\langle \vec{q}_\parallel \rangle$ and the accepted momentum range $\Delta q_\parallel$ of about 0.3 Å^{-1} for each experimental point. The measured cross section [Eq. (12) in Sec. III] is weighted over $\Delta q_\parallel$ by the "discrete probability densities" $f_{\Delta\Omega,h}$ that are reported for each parallel momenta under the bottom axis. In the measurements of Fig. 4, the variation of the centroid of the parallel momentum is negligible: $\langle q_\parallel(\Delta\theta)\rangle \approx \langle q_\parallel \rangle = 1.0$ Å^{-1} irrespective of the sequence adopted to model the interaction (single sequence event or double sequence event). On the contrary, the reconstructed perpendicular momentum depends on the sequence type.

With reference to Eqs. (8) and (9), upon the used kinematics, the normalization factor $(k_s k_e / k_0)$ and the density of the unbound states $\rho(\vec{k}_e)$ are constant for the measured DCSS, so the experimental angular distribution depends only on the kinematical factors and on the electron momentum density of the bound states ρ; according to Eqs. (9) and Eq. (12), it takes the form

$$\tilde{Y}_{(e,2e)}(\Delta\theta) \propto \tilde{\Gamma}_L \tilde{\rho}_L + \tilde{\Gamma}_{DL} \tilde{\rho}_{DL} + \tilde{\Gamma}_{LD} \tilde{\rho}_{LD}, \qquad (13)$$

where $\tilde{\Gamma}, \tilde{\rho}, = N_{tot}^{-1} \times \Sigma_h \Gamma_{t,h} \rho_{t,h}$, and t labels the three sequences *L*, *DL*, and *LD*. In the following paragraphs, we compare the experimental data with model calculations that include contributions from the single sequence event (*L*) or the double sequence event (*DL* and *LD*).

Single step (*L*) *event*. The (e,2e) mechanism is described by a single inelastic scattering event with a large momentum transfer. According to momentum and energy conservations, the experiment samples π valence-band states, with a minor contribution from σ_3 states, at fixed $q_\parallel$ and with perpendicular momentum ranging from 6.8 to 7.4 Å^{-1}. Momentum density calculations along q_z are available in literature only for the π and the σ_1 bands, and they are limited to the dependence along the ΓA direction[39,40]: Both distributions become nearly constant for momentum values $q_z > 3$ Å^{-1}. On this basis, we may expect that the π and the σ_3 states contribute with constant electron momentum densities to the measured cross section, which becomes proportional only to the kinematical factor $\tilde{\Gamma}_L$ [see Eq. (13)]. According to the approximations used in Sec. II, this factor is the Fourier transform of the electron-electron potential $\tilde{W}_{se}$, which varies as the inverse fourth power of the momentum transfer. Hence, the DCSS varies monotonically with $\Delta\theta$ in the measured angular range. The calculated distribution is reported in Fig. 4 (dot-dashed line); it decreases monotonically as $\Delta\theta$ increases and it is in evident disagreement with the measured profile.

Double-step (*LD*, *DL*) *event*. In this case, the inelastic scattering in each sequence is characterized by small momentum transfer, and we will also distinguish cases in which *L* and *D* act as coherent or incoherent processes. The present measurements do not allow a discrimination of the contribution of the two sequences; hence, the experimental data are compared with the sum (average) of the contributions of both sequences. On the basis of Ref. 29, the two contributions have the same weight. The variation of q_z (from 2.1 to 2.7 Å^{-1}) selected by the two sequences is such that the associated momentum distribution variations almost compensate each other. The measured momentum density extrapolated from calculations along the ΓA direction[39,40] results in variation less than 20% over the angle scan.

In the case of events acting coherently in each sequence, according to Eqs. (9) and (13), the measured (e,2e) cross section reduces to

$$\widetilde{Y}_{DL\cup LD}(\Delta\theta)=\widetilde{Y}_{DL}(\Delta\theta)+\widetilde{Y}_{LD}(\Delta\theta)\propto\widetilde{\Gamma}_{DL}\rho_{DL}(q_z)+\widetilde{\Gamma}_{LD}\rho_{LD}(q_z). \qquad (14)$$

To perform the calculation of the kinematical factors, we have used the same electron-electron potential W_{se} as in the case of the single step (L event) and assumed the crystal potential V_s as a superposition of effective core potentials of the ions $V_{ion}(\vec{\mathbf{r}})$ with a functional form corresponding to a Coulomb potential (neglecting the screening length: $\lambda_{eff}=0$ Å).[18] To fit the experimental data, we have used only a scale factor as a free parameter. The calculated distribution (solid line in Fig. 4) is in fair agreement with the measured distribution.

In the case of "incoherent" processes [Eq. (10)], the coincidence cross section corresponding to each sequence is the product of two independent scatterings, and according to Eq. (13) it reduces to the form

$$\widetilde{Y}_{DL\cup LD}(\Delta\theta)\propto\widetilde{\Gamma}_{D}\widetilde{\Gamma}_{L}\rho_{DL}(q_z)+\widetilde{\Gamma}_{D}\widetilde{\Gamma}_{L}\rho_{LD}(q_z), \qquad (15)$$

where $\widetilde{\Gamma}_D$ and $\widetilde{\Gamma}_L$ are the kinematical factors of the electron-electron elastic and inelastic scattering, respectively. The calculated distribution (dashed line in Fig. 4) reproduces only the gross features of the measured one: It shows a maximum in the vicinity of the specular direction; however, it is much broader and asymmetric with respect to the experimental distribution, and the peak position is shifted by ≈−1°.

To summarize, these findings clearly suggest that in describing electron scattering in reflection geometry at intermediate energies, it is crucial to adopt not too simple a picture of the electron interaction with the solid. A single-event mechanism as sole does not explain the experimental curve, but it may make a very small contribution. Double-event models in general give a good description of the experiment. When the elastic and inelastic events are considered as incoherent, as already done in Ref. 21 only a qualitative agreement with the angle dependence of the measured DCSS is obtained. A much better agreement is obtained when, within a given sequence, the elastic and inelastic events are treated coherently.

B. Band mapping measurements

According to the coherent model described by Eq. (9), the measured (e,2e) cross section reduces to the form

$$\widetilde{Y}_{(e,2e)}(E_B,\vec{q})\propto A\cdot[\widetilde{\Gamma}_{DL}+\widetilde{\Gamma}_{LD}]\widetilde{\rho}(\varepsilon,q_{\parallel},q_z), \qquad (16)$$

which explicitly highlights the dependence of the electron momentum density on both binding energy and recoil momentum. To bring the measured cross section onto the same relative scale, we have divided each of them for the factor A, which depends on the experimental conditions and on the momentum density of the ejected electron. Namely,

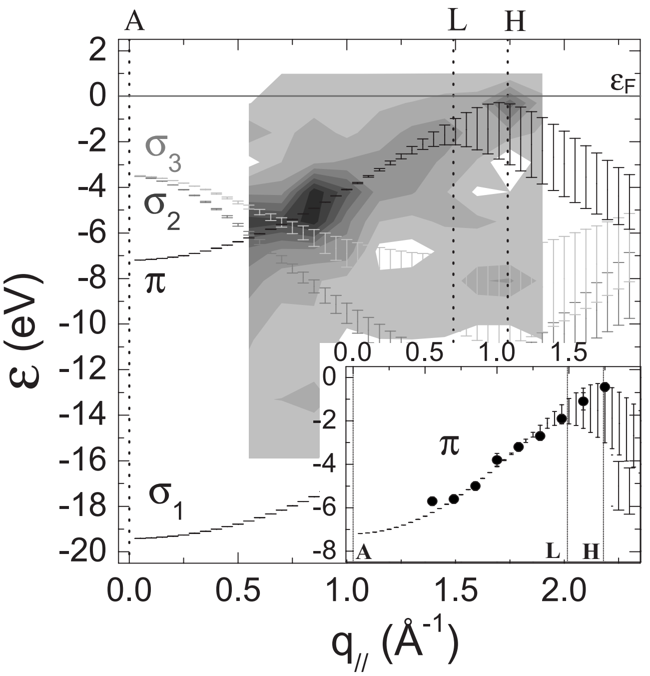

FIG. 5. Experimental (e,2e) cross section plotted in the binding energy–parallel momentum phase-space after energy-loss deconvolution. The intensities are given by a linear gray scale (darker regions correspond to higher intensities). The binding energy is relative to the Fermi level ε_F. The HOPG valence-band structure is also shown (see text for explanation). In the inset, the dispersion of the centroid values (squares) obtained by the fitting procedure is compared with the dispersion ribbons $f(q_{\parallel},\varepsilon)$ of the HOPG π states.

$$A=\frac{k_s k_e}{k_0}\cdot\widetilde{\rho}(\vec{k}_e)\cdot f_{CMA}(E_e)f_{HDA}(E_0,E_s), \qquad (17)$$

where f_{CMA} and f_{HDA} are the efficiency functions of the two-electron analyzers, which have been derived by an independent set of calibration measurements and whose details can be found in Ref. 37; the modulation due to the unoccupied density of states has been estimated by SEE measurements.[34] Once A is determined, we are left with quantities that depend only on sample properties that can be compared directly with calculated band structures. This is done in Fig. 5, where the intensity of the $\widetilde{Y}_{(e,2e)}/A$ ratio is reported as a gray-scale map after multiple loss deconvolution.[19] The binding energy is relative to the Fermi level ε_F. Darker regions represent higher intensities, while the blank regions are the unmeasured part of the $(q_{\parallel},\varepsilon)$ space. For a homogeneous visualization, the plotted intensities are obtained by interpolating the data at a constant step of 0.05 Å^{-1}, weighting each experimental point by the function $f_{\Delta\Omega,h}$, three points averaging.

In Fig. 5, we have displayed the valence-band structure of HOPG calculated in the *ALH* plane, obtained by averaging over all the azimuth orientations of graphite high symmetry directions. Starting from the band calculations of Ref. 40

performed in the ΓKM plane and along the ΓA direction of single-crystal graphite (0001), we have projected the bands over the ALH plane. Because of the in-plane average of the crystallites, in HOPG the in-plane Brillouin zone boundaries are not univocally determined, and for the same reason families, rather than individual dispersion curves, will correspond to each $q_\parallel$. The interval of binding energies upon which these families are distributed is represented by "ribbons" in Fig. 5.

From the contour lines of Fig. 5, we note that the energy dispersion of the π states is well reproduced by the measured cross section, with a region of maximum intensity between 0.6 and 0.9 Å^{-1}. In particular, it is evidently a maximum close to the boundary point H, whose position ($q_F^{exp} = 1.7 \pm 0.1$ Å^{-1}) agrees with the Fermi momentum of graphite.[41] This momentum distribution is relative to states located near the Fermi level ($\varepsilon = -0.2$ eV), for which the distortion effects due to multiple scattering are minimal; this result can be considered a further experimental check to corroborate the validity of our kinematical reconstruction. To make the comparison with theory more quantitative, we have fitted each experimental energy distribution for each parallel momentum by a free Gaussian function. In the inset of Fig. 5, the dispersion of the centroid values (squares) obtained by the fitting procedure is reported and compared with the "dispersion ribbons" of the π states. The agreement between theory and experiment is satisfactory and confirms the appropriateness of the $q_\parallel$-reconstruction procedure adopted.

As along the z direction the valence states have an atomiclike behavior, in Fig. 5 we have plotted the measured cross section as a function of the parallel momentum regardless of the q_z component. According to the two-dimensional structure of HOPG, we propose to decouple the parallel and the perpendicular components of the spectral momentum density for each selected orbital. Hence, momentum density takes the form of the product of the two spectral components: $\rho = \rho_\parallel \times \rho_z$. By using Eq. (16), we obtain the spectral parallel momentum density,

$$\tilde{\rho}_\parallel(\varepsilon, q_\parallel)\big|_{q_z} \propto \tilde{\rho}_z^{-1} \frac{\tilde{Y}'_{(e,2e)}(\varepsilon, \vec{q})}{[\tilde{\Gamma}_{DL} + \tilde{\Gamma}_{LD}]}, \qquad (18)$$

where $\tilde{\rho}_z$ does not depend on the binding energy and where $\tilde{Y}'(\varepsilon)|_{q_\parallel, q_z}$ is the separation energy spectrum at fixed momentum value. In Fig. 6, the densities of states $\tilde{\rho}(\varepsilon)|_{q_\parallel, q_z}$ are reported (squares). They correspond to different momentum values in the range $(0.55 < q_\parallel < 1.75)$ Å^{-1} and are derived from Eq. (18) upon operating an energy binning $\Delta E_{bin} = 1.3$ eV on each measurement. Fifteen distributions are shown in the figure; they are arranged in three columns, each one corresponding to the perpendicular momentum selected in the measurement. The kinematical factor of each measurement depends weakly on the momentum (about 10%), while it varies by about a factor of 10 over the energy range, this large variation enhancing the uncertainty on the determination of deeper-lying states.

To extract the momentum density for each individual valence state, we have fitted the measured intensity with a function given by the sum (thick line) of Gaussian curves (thin lines for each individual electron state: dotted lines for π states and continuous ones for σ_2 and σ_3). The only free parameter is the amplitude; the energy positions of the Gaussians are taken from calculations of Ref. 40 and the full widths at half maxima obey the following expression: $\sqrt{(\Delta E_{bin})^2 + (\Delta E_{disp})^2 + (\Delta E_\tau)^2}$, in which ΔE_{disp} is the energy state dispersion corresponding to the projection of the momentum acceptance onto the energy axis and ΔE_τ is the intrinsic lifetime of the bound state that we have considered proportional to the square root of the binding energy. The distribution intensities decrease for increasing parallel momentum. For each fixed momentum value, the main feature corresponds to π states, while less intense structures are associated with σ_2 and σ_3 states. For small parallel momentum values, the three states are not well resolved. For increasing momentum, the energy separation increases, and in the distributions at $q_\parallel = 1.00$ Å^{-1} we can clearly distinguish π and σ_2 states. For $q_\parallel > 1.00$ Å^{-1}, the sampled energy range allows us to measure only π states. The fit functions reproduce the gross features of the experimental distributions, except for deep binding energies; this finding is quite evident in the distributions for $q_\parallel < 0.7$ Å^{-1}. The difference between the

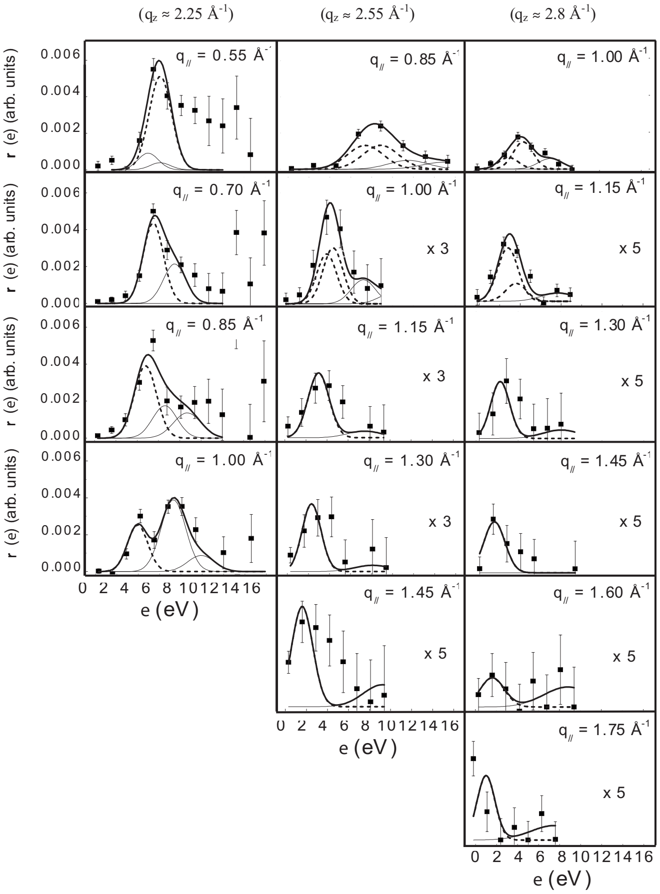

FIG. 6. Densities of states corresponding to different values of the recoil parallel momenta $(0.55 \leq q_\parallel \leq 1.75)$ Å^{-1}, displayed at a momentum step of 0.15 Å^{-1} and for three different q_z values. The experimental distributions (dots) are fitted by three Gaussian curves (thin lines) for each individual electron state (dotted lines for π states; continuous ones for σ_2 and σ_3) with centroids and widths given by theory (Ref. 40).

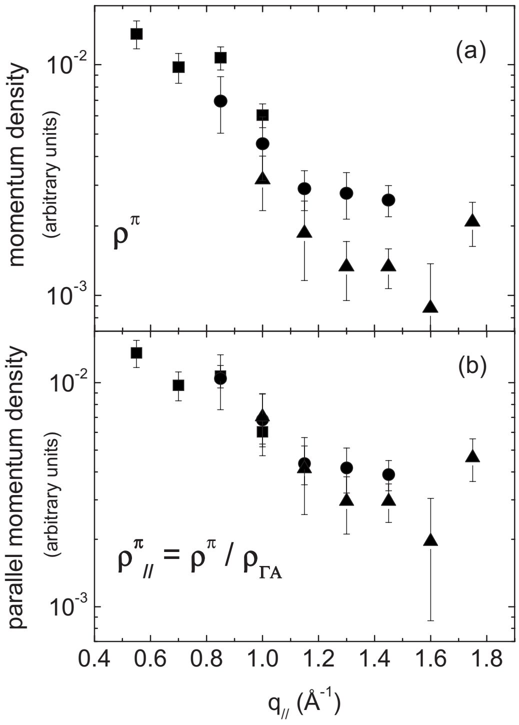

FIG. 7. (a) Electron momentum distributions of the HOPG π states measured for three q_z values of 2.25 Å^{-1} (squares), 2.55 Å^{-1} (circles), and 2.8 Å^{-1} (triangles). (b) Parallel momentum density of the π states obtained by dividing each measured distribution by the momentum density along the ΓA direction calculated in Ref. 35.

measured and the fitted intensities could be ascribed both to intrinsic loss contributions,[42] which are not accounted by the deconvolution procedure, and to $\vec{g}$-assisted events, which bring intensities associated with σ_2 and σ_3 bands into the first Brillouin zone. For such events, the measured momentum is a "crystal momentum:" $\vec{q}\,'=\vec{q}+n\vec{g}$, where n is an integer number. These are anyway minority events (we notice the multiplicative factors used for the spectra at large q values to bring the corresponding densities of states to the same relative scale) with respect to the dominant signal given by π-band states in the first Brillouin zone.

Statistical uncertainty limits to the π band a reliable analysis of the momentum dependence. The distributions corresponding to the three selected q_z values are reported in Fig. 7 (squares, circles, and triangles, respectively). We can notice that in the $q_{\parallel}$-overlap regions the distributions show similar intensities in spite of corrections for the different kinematical factors [Fig. 7(a)]. According to Eq. (18), the spectral parallel momentum density of the π states is obtained by dividing each measured distribution by the momentum density along the ΓA direction: $\tilde{\rho}_{\parallel}(q_{\parallel})=\tilde{\rho}(q)/\tilde{\rho}_{\Gamma A}(q_z)$. The result is reported in Fig. 7(b), where we have used for $\tilde{\rho}_{\Gamma A}(q_z)$ the distribution calculated in ref. 40

Experimental results shown in Fig. 7(a) suggest a clear dependence of the measured momentum distributions upon the perpendicular component q_z, and matching between the three distributions is achieved by taking into account the dependence on q_z [Fig. 7(b)]; hence, we argue that the reflection (e,2e) cross section depends on the full real momentum rather than only on the parallel component $q_{\parallel}$ of crystal momentum. The improved match obtained in the overlap regions corroborates the validity of our approximation decoupling the perpendicular and the parallel momentum densities in HOPG; in fact, the momentum distributions link up well, though different kinematics conditions characterize them. The experimental profile is a measurement of the parallel momentum density, obtained in spite of the presence of a non-negligible perpendicular component. Namely, the comprehension of the reflection (e,2e) mechanism has allowed us to measure $\rho(\pi)$ as a function of $\vec{q}_{\parallel}$ in the first Brillouin zone and of q_z determined by the momentum transferred in the inelastic collision rather than by reciprocal lattice vectors $\vec{g}$. To make the reflection (e,2e) technique a reliable method, a comparison with specific calculations is needed. An improved statistics for measurements at deeper binding energies is also required in order to evaluate the relevance of multiple scattering and of $\vec{g}$-assisted events.

V. CONCLUSIONS

This paper answers the question of which model is appropriate to describe grazing incidence (e,2e) events from surfaces at moderate energies and in asymmetric kinematics. To this end, the differential cross section for reflection (e,2e) processes has been derived within two different frameworks based on the theoretical models developed in Refs. 21 and 24. Both cross sections rely on a two-step mechanism that couples, either coherently or incoherently, the elastic collision with the crystal lattice to the ionizing inelastic one. To highlight which of the two models reproduces better the mechanism of the electron pair ejection, the cross section dependence on momentum transfer at grazing incidence angle has been experimentally investigated. Experimental results rule out the possibility of describing these events as a single inelastic collision with large momentum transfer. Double-step models, in which the inelastic scattering occurs at small momentum transfer, give in general a correct description of the experiment; in particular, the fair agreement obtained between measurements and theory in the "coherent" case gives evidence that such description is preferable over the incoherent one.

In reflection geometry, it has been possible to perform valence-band mapping and to extract electron momentum density with energy and momentum resolutions (1.3 eV, 0.15 Å^{-1}) that are comparable with those obtained in transmission geometry (e,2e) spectroscopy. In the case of HOPG, the aforementioned coherent two-step model has allowed us to measure the momentum distribution of π-electron states in the first Brillouin zone. The agreement between theory and experiment is satisfactory, but the presence of $\vec{g}$-assisted events cannot be excluded.

It is worth noticing that we have applied reflection (e,2e) spectroscopy in low-energy conditions, but it could as well be applied at much higher incident energies. Hence, in principle, by tuning the energy one can achieve either bulk or surface sensitivity. The results of the present work, obtained by an implemented apparatus that has allowed performing the experiments with significant reduction of the acquisition times, show that the determined model for reflection (e,2e) can be used to measure momentum densities, thus opening up the possibility to build a momentum spectroscopy with high surface sensitivity that makes this technique an appealing method for studying surfaces and overlayer systems.

ACKNOWLEDGMENTS

The authors are indebted to J. Berakdar for stimulating discussions and a critical reading of the manuscript.

---

*Corresponding author.

[1] I. E. McCarthy and E. Weigold, *Electron Momentum Spectroscopy* (Kluwer Academic, Dordrecht/Plenum, New York, 1999).

[2] I. E. McCarthy and E. Weigold, Rep. Prog. Phys. **51**, 299 (1988).

[3] M. A. Coplan, J. H. Moore, and J. P. Doering, Rev. Mod. Phys. **66**, 985 (1994).

[4] C. E. Brion, G. Cooper, Y. Zheng, I. V. Litvinyuk, and I. E. McCarthy, Chem. Phys. **270**, 13 (2001).

[5] Malcolm J. Cooper, Peter E. Mijnarends, Nobuhiro Shiotani, Nobuhiko Sakai, and Arun Bansil, *X-ray Compton Scattering* (Oxford University Press, New York, 2004).

[6] I. Kanazawa, S. Tanigawa, R. Suzuki, M. Sano, and H. Inokuchi, Phys. Rev. B **42**, 11583 (1990).

[7] T. Sattler, Th. Tschentscher, J. R. Schneider, M. Vos, A. S. Kheifets, D. R. Lun, E. Weigold, G. Dollinger, H. Bross, and F. Bell, Phys. Rev. B **63**, 155204 (2001).

[8] M. Vos and I. E. McCarthy, Rev. Mod. Phys. **67**, 713 (1995).

[9] S. Hüfner, in *Photoelectron Spectroscopy*, Springer Series in Solid-State Science, Vol. 82, edited by M. Cardona, P. Fulde, K. von Klitzing, and H.-J. Queisser (Springer-Verlag, Berlin, 1995).

[10] M. Vos, A. S. Kheifets, and E. Weigold, J. Phys. Chem. Solids **62**, 2215 (2001).

[11] C. Bowles, A. S. Kheifets, V. A. Sashin, M. Vos, and E. Weigold, J. Electron Spectrosc. Relat. Phenom. **141**, 95 (2004).

[12] A. L. Ritter, J. R. Dennison, and R. Jones, Phys. Rev. Lett. **53**, 2054 (1984); X. Guo, Z. Fang, A. S. Kheifets, S. A. Canney, M. Vos, I. E. McCarthy, and E. Weigold, Phys. Rev. B **57**, 6333 (1998), and references therein.

[13] S. Iacobucci, L. Marassi, R. Camilloni, S. Nannarone, and G. Stefani, Phys. Rev. B **51**, R10252 (1995).

[14] H. Luth, *Surfaces and Interfaces of Solids* (Springer-Verlag, Berlin, 1993).

[15] A. Liscio, R. Gotter, A. Ruocco, S. Iacobucci, A. G. Danese, R. A. Bartynski, and G. Stefani, J. Electron Spectrosc. Relat. Phenom. **87**, 505 (2004).

[16] W. S. M. Werner, W. Smekal, H. Stori, H. Winter, G. Stefani, A. Ruocco, F. Offi, R. Gotter, A. Morgante, and F. Tommasini, Phys. Rev. Lett. **94**, 038302 (2005).

[17] J. B. Pendry, *Low Energy Electron Diffraction* (Academic, London, 1974).

[18] J. Berakdar and M. P. Das, Phys. Rev. A **56**, 1403 (1997).

[19] S. Rioual, S. Iacobucci, D. Neri, A. S. Kheifets, and G. Stefani, Phys. Rev. B **57**, 2545 (1998).

[20] A. Morozov, J. Berakdar, S. N. Samarin, F. U. Hillebrecht, and J. Kirschner, Phys. Rev. B **65**, 104425 (2002).

[21] A. S. Kheifets, S. Iacobucci, A. Ruocco, R. Camilloni, and G. Stefani, Phys. Rev. B **57**, 7360 (1998).

[22] S. Iacobucci, L. Marassi, R. Camilloni, B. Marzilli, S. Nannarone, and G. Stefani, J. Electron Spectrosc. Relat. Phenom. **76**, 109 (1995).

[23] O. M. Artamonov, S. N. Samarin, and J. Kirschner, Appl. Phys. A: Mater. Sci. Process. **A65**, 535 (1997).

[24] K. A. Kouzakov and J. Berakdar, Phys. Rev. B **66**, 235114 (2002).

[25] S. Y. Zhou, G.-H. Gweon, and A. Lanzara, Ann. Phys. (N.Y.) **321**, 1730 (2006).

[26] M. Grioni, Ch. R. Ast, D. Pacilè, M. Papagno, H. Berger, and L. Perfetti, New J. Phys. **7**, 106 (2005).

[27] S. Iacobucci, S. Rioual, A. Ruocco, M. Mastropietro, and G. Stefani, Surf. Sci. **454**, 1026 (2000).

[28] In a specific formulation for solid systems, this corresponds to approximate the spectral function with a delta function in the momentum space (see, for instance, Ref. 9).

[29] A. Ruocco, M. Milani, S. Nannarone, and G. Stefani, Phys. Rev. B **59**, 13359 (1999).

[30] A. Bianconi, S. B. M. Hagström, and R. Z. Bachrach, Phys. Rev. B **16**, 5543 (1977).

[31] V. N. Strocov, A. Charrier, J. M. Themlin, M. Rohlfing, R. Claessen, N. Barrett, J. Avila, J. Sanchez, and M. C. Asensio, Phys. Rev. B **64**, 075105 (2001).

[32] M. Vos, P. Storer, Y. Q. Cai, I. E. McCarthy, and E. Weigold, Phys. Rev. B **51**, 1866 (1995).

[33] M. Bovet, V. N. Strocov, F. Clerc, C. Koitzsch, D. Naumović, and P. Aebi, Phys. Rev. Lett. **93**, 107601 (2004).

[34] A. Liscio, Ph.D. thesis, Rome, 2004.

[35] J. J. Sakurai, *Modern Quantum Mechanics* (Addison-Wesley, New York, 1994).

[36] G. Stefani, L. Avaldi, and R. Camilloni, in *New Directions in Research with Third Generation Soft X-ray Synchrotron Radiation Sources*, NATO Advanced Studies Institute, Series E: Applied Science, edited by U. Meyer, R. Doezner, A. F. Schlachter, and F. J. Wuilleumier (Kluwer Academic, Dordrecht, 1994), Vol. 254, pp. 161–190.

[37] A. Liscio, A. Ruocco, G. Stefani, and S. Iacobucci, J. Electron Spectrosc. Relat. Phenom. **161**, 140 (2007).

[38] G. Musket, W. Mc Lean, C. A. Colmenares, D. Makowiecki, and W. J. Siekhaus, Appl. Surf. Sci. **10**, 143 (1982).

[39] C. Gao, A. L. Ritter, J. R. Dennison, and N. A. W. Holzwarth, Phys. Rev. B **37**, 3914 (1988).

[40] A. S. Kheifets and M. Vos, J. Phys.: Condens. Matter **7**, 3895 (1995).

[41] N. W. Ashcroft and I. Mermin, *Solid State Physics*, international ed. (Saunders College, Fort Worth, 1976).

[42] N. A. Krasil'Nikova and N. M. Persiantseva, Phys. Lett. **69A**, 287 (1978).